Imaging diamond with x-rays

2009 J. Phys.: Condens. Matter 21 364217

(http://iopscience.iop.org/0953-8984/21/36/364217)

J. Phys.: Condens. Matter **21** (2009) 364217 (15pp) doi:10.1088/0953-8984/21/36/364217

Imaging diamond with x-rays

Moreton Moore

Department of Physics, Royal Holloway University of London, Egham, Surrey TW20 0EX, UK

E-mail: m.moore@rhul.ac.uk

Received 5 April 2009
Published 19 August 2009
Online at stacks.iop.org/JPhysCM/21/364217

Abstract
The various techniques for imaging diamonds with x-rays are discussed: x-radiography, x-ray phase-contrast imaging, x-ray topography, x-ray reciprocal-space mapping, x-ray microscopy; together with the characterization of the crystal defects which these techniques reveal.

1. Introduction

X-rays may be used to image whole diamonds, or selected regions, by radiography or by using various techniques employing a Bragg reflection for x-ray diffraction contrast. The x-rays may be chosen to be parallel or divergent, to have a broad range of wavelengths or to be monochromatic. They may be produced from conventional metal targets or from a synchrotron. The various possibilities are discussed in this review.

2. X-rays

It is well known that x-rays are a form of electromagnetic radiation of short wavelength, discovered by Wilhelm Roentgen in 1895. Their wavelengths span a wide range, which may be sub-divided (somewhat arbitrarily) into hard x-rays of approximately 0.01–0.1 nm and soft x-rays of 0.1–10.0 nm. The angstrom unit is still in popular use: 1 Å = 0.1 nm = 10^{-10} m. These wavelengths correspond to energies (in kilo-electron-volts, $E = hc/\lambda$, h = Planck's constant, c = velocity of light) of 124–12.4 keV for hard x-rays; and 12.4–0.124 keV for soft x-rays. The range for soft x-rays (a factor of 100) is thus ten times as wide as that for hard x-rays (a factor of 10), but it should be emphasized that these are just convenient numbers and are open to further discussion.

X-rays may be produced by accelerating electrons, of energies in the above ranges, towards a metal target (positive electrode). The abrupt stoppage of electrons by the atoms in the target converts these high energies into the emission of x-rays. The spectrum is broad, but with a sharp cut-off at the short wavelength end, corresponding to the accelerating voltage applied. This radiation is sometimes called Bremsstrahlung (breaking radiation). The metal target may be static, as in a sealed x-ray tube; or moving, as in a rotating-anode x-ray generator. In addition, at sufficiently high voltages, there may also be sharp characteristic peaks superimposed upon the continuous spectrum, characteristic of the target material. These come from the brief promotion of electrons dislodged from target atoms to discrete higher energies. These (or other) electrons drop back to their original energies and, in so doing, emit x-rays of a particular energy (or particular wavelength). Kα radiation arises from electrons dropping back to the K-shell from the L-shell; and Kβ radiation from those transferring between the M- and K-shells. There are only a few such allowed transitions (grouped into series) associated with each elemental metal and they give rise to very intense narrow peaks (often called 'lines') in the spectrum. The Kβ radiation may be filtered out by a thin metal foil (such as 20 μm of Ni for Cu Kβ, or 100 μm of Zr for Mo Kβ) which halves the intensity of Kα but reduces the Kβ to less than 1%. Such radiation is not exactly monochromatic but it is nevertheless useful for many simple applications. To achieve monochromatic radiation, one or more Bragg reflections from crystals are employed.

Synchrotron radiation is a continuous electromagnetic spectrum extending from x-rays, through ultra-violet, the narrow visible range, infrared and beyond to radio waves. By analogy with the visible spectrum of many colours, a broad continuous range of x-rays is called 'white', in distinction from 'monochromatic'. This radiation is produced by accelerating charged particles (usually electrons) at speeds close to the speed of light on a curved path in a magnetic field. The radiation is emitted mainly in the forwards direction within a very narrow cone of angle typically a fraction of a milliradian. The angle is approximately mc^2/E, where m is the rest mass of the electron and $mc^2 = 0.511$ MeV. Thus, for an electron energy $E = 2$ GeV, this angle is 0.25 mrad, (equivalent to a vertical height of 10 mm at a distance of 40 m). The magnetic fields may simply turn the electrons through a gently curved path (from a bending magnet) or cause the electrons to move through paths of smaller radius of curvature (from wigglers and undulators) [1].

Table 1. Transmission of x-rays of various wavelengths through diamond. (Note: the wavelengths (λ) of four characteristic Kα emissions from silver, molybdenum, copper and chromium are given. Values for the mass absorption coefficient (μ) are listed for these wavelengths together with two popular wavelengths from synchrotron radiation. (ρ is the density of diamond.) The transmission of such x-rays through various thicknesses (t) of diamond are given in the lower four rows.)

Radiation	Ag Kα	Mo Kα	Synch.rad.	Cu Kα	Synch.rad.	Cr Kα
λ (nm)	0.056	0.071	0.100	0.154	0.200	0.229
Energy (keV)	22.1	17.4	12.4	8.04	6.20	5.41
μ/ρ (cm^2 g^{-1})	0.374	0.576	1.32	4.51	9.86	15.0
μ (cm^{-1})	1.315	2.025	4.640	15.85	34.66	52.73
$t = 0.3$ mm	0.96	0.94	0.87	0.62	0.35	0.21
$t = 1.0$ mm	0.88	0.82	0.63	0.20	0.031	5.1×10^{-3}
$t = 3.0$ mm	0.67	0.54	0.25	8.6×10^{-3}	3.1×10^{-5}	1.4×10^{-7}
$t = 10.0$ mm	0.27	0.13	9.7×10^{-3}	1.3×10^{-7}	8.9×10^{-16}	1.3×10^{-23}

At an experimental station designed for hard x-rays, the radiation usually emerges from a beryllium window on the end of an evacuated beam-pipe; and therefore a long wavelength limit of 0.25 nm is set both by the window material and by absorption in air thereafter. The spectrum on the short wavelength side of maximum intensity falls off steeply. The useful wavelength range from a bending magnet extends from about 0.05 to 0.25 nm, giving a factor of 5 in wavelength. A wiggler magnet makes the electron-beam curve more sharply and the entire x-ray spectrum is shifted to shorter wavelengths: the range is increased to approximately 0.01–0.25 nm: (a factor of 25).

There are many advantages of synchrotron radiation [2] as will be discussed later. Apart from the wide range of x-ray energies (wavelengths) available, the narrow divergence (excellent collimation), the high intensity (giving short exposure times), the linear polarization and the pulsed time structure are all useful for particular experiments. And as far as diamond is concerned, radiation damage is not usually evident in the relatively short exposure times used for imaging.

3. Radiography: x-ray absorption

The iconic x-ray image of the hand of Roentgen's wife is certainly the earliest x-ray picture of rings, but it is probably not the earliest such picture of a diamond. Within the strong absorption contrast of the metals, it is not obvious whether either ring contained any gems. Today, x-ray absorption contrast is used worldwide in hospitals, in airport luggage inspection and in many other applications. The great penetration power of x-rays is used for the non-destructive imaging of otherwise inaccessible interiors of various objects. Diamond, of low atomic number, is particularly transparent to x-rays.

The intensity I of a beam of x-rays transmitted through a specimen of thickness t is given by

$$I = I_0 \exp(-\mu t) \tag{1}$$

where I_0 is the intensity of the incident beam and μ is the linear absorption coefficient. In table 1, data for four popular laboratory radiations (from silver, molybdenum, copper and chromium) are given, together with two wavelengths from synchrotron radiation. The last four rows give values of the transmission I/I_0 for various thicknesses of diamond, taking the density ρ of diamond as 3.515 g cm^{-3} and values of μ/ρ from [3]. One can see that it does not take much diamond to absorb the less energetic x-rays. One millimetre of diamond transmits just one-fifth of Cu Kα radiation but only a half of one per cent of Cr Kα radiation.

X-rays are also absorbed in air. Ten centimetres of air transmits 99% of Mo Kα and 89% of Cu Kα, but only 68% of Cr Kα. One metre of air transmits 90% of Mo Kα, 31% of Cu Kα and only 2% of Cr Kα radiation.

Radiography usually employs a divergent beam from a small distant source. For the best resolution and least distortion, the specimen is placed close to, or in contact with, the photographic film. Sometimes cracks in gem diamonds are filled with an optically transparent material of high refractive index (such as lead glass or silicone oil) but which is more absorbent to x-rays than the diamond. X-radiography can therefore be used to reveal such filled cracks, especially if several different views are taken with x-rays of low energy.

4. X-ray phase-contrast imaging

When a specimen, such as diamond, is made of light elements ($Z \leqslant 8$), it hardly absorbs x-rays of wavelength of, say, 0.15 nm (energy 8 keV); so conventional radiography is rather lacking in contrast. Image formation in x-ray phase contrast is similar to visible-light optical phase-contrast microscopy. Contrast arises from the phase gradients in the transmitted beam, caused by refractive index variations in the specimen or by refraction on the object surface itself [4]. For polycrystalline diamond specimens with rough surfaces, the surface morphology and cracks dominate the phase-contrast images [5].

The spatial coherence length L of a beam of x-rays of wavelength λ is given by

$$L = \lambda/2\gamma, \tag{2}$$

where γ is the small angle subtended by a distant source. For example, at the former CLRC Daresbury Topography Station 7.6, the vertical source size of 0.35 mm at a distance of 80 m, gave an angle $\gamma = 4.375$ μrad (=0.9 arcseconds). Thus, for a typical wavelength of 0.1 nm (=1 Å), L was 11 μm. Variations in the optical path length of the x-rays, or phase variations

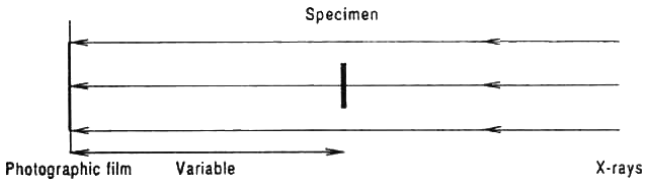

Figure 1. Simple experimental arrangement: the specimen is illuminated by the direct synchrotron beam and the image is recorded in transmission (at a variable distance) on the photographic film. Reproduced with permission from [5]. Copyright 1999, IOP Publishing Ltd.

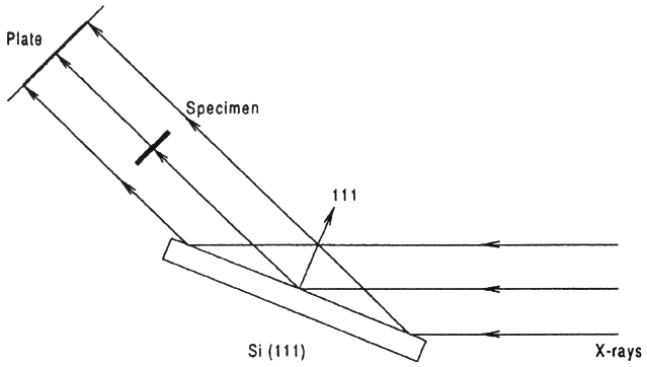

Figure 2. A single Bragg reflection from a perfect silicon crystal selects one wavelength (and its harmonics) from the synchrotron beam. Reproduced with permission from [5]. Copyright 1999, IOP Publishing Ltd.

Table 2. Refractive index decrement and full-wave plate thickness for diamond. (Note: values of the refractive index decrement $\delta \times 10^6$ are listed for various wavelengths, together with the thicknesses (t) of diamond needed to cause a phase advance of 2π.)

Radiation	W Kα_1	Ag Kα_1	Mo Kα_1	Cu Kα_1	Cr Kα_1
λ (nm)	0.021	0.056	0.071	0.154	0.229
$10^6\delta$	0.21	1.5	2.4	11.3	25.0
t (μm)	101	38	30	14	9.2

across the beam, cause contrast by Fresnel diffraction. The refractive index n for x-rays is slightly smaller than unity by a term of order 10^{-6} for most materials. Let $\delta = 1-n$ be the real part of the refractive index decrement for x-rays of wavelength λ; then the phase change φ produced by a uniform specimen of thickness t, is given by

$$\varphi = 2\pi t\delta/\lambda. \tag{3}$$

In table 2, values of the thickness t of diamond (carbon) needed to cause a phase advance of 2π are given [5].

The simplest experimental arrangement for imaging is shown in figure 1, where only the specimen is placed in the direct synchrotron beam, and the transmitted beam is recorded on a photographic plate or film. In conventional radiography, the specimen and film are in close contact; but for phase-contrast imaging, they are widely separated.

By introducing a perfect crystal of, for example, silicon, into the experiment to reflect the x-rays (see section 5), the photographic film is no longer in the direct beam: see figure 2. This lowers the background intensity considerably, improves the contrast and filters out most of the white beam. The crystal allows only a very limited energy range around the chosen energy (wavelength λ) to be reflected, together with any harmonics ($\lambda/2$, $\lambda/3$, $\lambda/4$, etc).

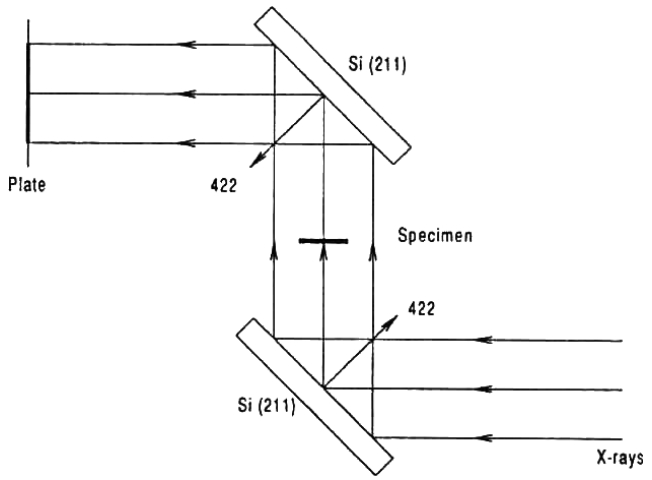

Figure 3. Double-crystal arrangement. Reproduced with permission from [5]. Copyright 1999, IOP Publishing Ltd.

A second crystal may be used to analyse the beam coming through the specimen: see figure 3. Here two symmetrical reflections are used for highly collimated synchrotron radiation. In this context, 'symmetrical' means that the incident and Bragg reflected x-rays make equal angles with the specimen surface. The lower crystal selects a single wavelength (plus harmonics) from the white synchrotron beam. The reflected beam then passes through the specimen. By adjusting the upper crystal through small angles either side of the Bragg reflection, image contrast can be altered and even reversed (black to white and vice versa): see figure 4. The specimen is a thin plate of polycrystalline synthetic diamond grown by chemical vapour deposition (CVD). The analyser crystal has been turned through 2.5 s of arc between taking the two pictures. (1 arcsecond = 4.85 μrad = the angle subtended by a 2-pence coin at a distance of $3\frac{1}{4}$ miles.)

5. X-ray diffraction

At the suggestion of Max von Laue, the first x-ray diffraction photograph was taken in 1912 by Walter Friedrich and Paul Knipping of a copper sulfate crystal. Laue also formulated the diffraction equations that bear his name and he received the Nobel Prize for Physics in 1914. The x-rays had a range of wavelengths and the resulting diffraction pattern was recorded photographically. Sir Lawrence Bragg considered the x-rays to be simply reflected from parallel planes of atoms in the crystal lattice; and he and his father, Sir Henry Bragg, deduced the crystal structures of many substances, including diamond [6], and together they won the Nobel Prize in 1915.

Bragg's law

$$2d\sin\theta = n\lambda \tag{4}$$

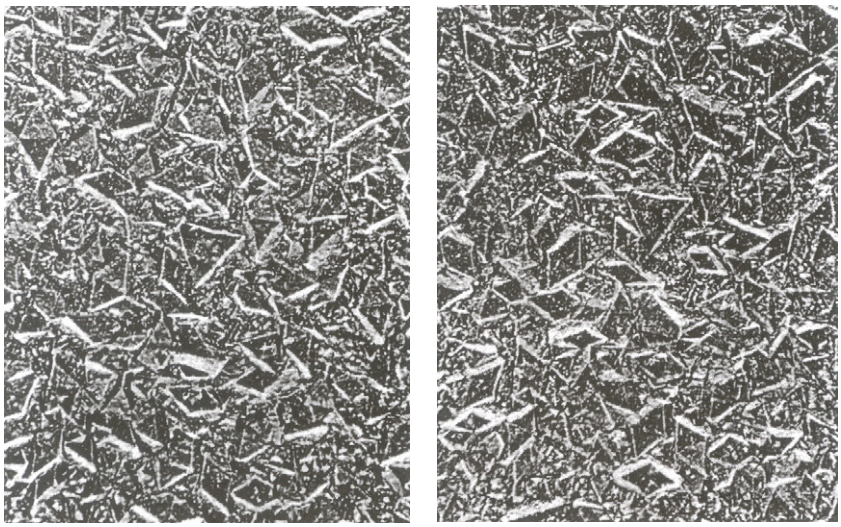

Figure 4. Example of CVD diamond imaged by x-ray phase contrast, image width = 2.5 mm. The analyser crystal has been turned through 2.5 s of arc between taking the two pictures. Reproduced with permission from [5]. Copyright 1999, IOP Publishing Ltd.

gives the Bragg angle (θ) at which an x-ray beam of wavelength λ will be strongly reflected by parallel planes of atoms ('Bragg planes') of separation d in a crystal. n is the order of reflection (1, 2, 3, ...). For white radiation, the harmonics $\lambda/2$, $\lambda/3$, etc may also be reflected at the same Bragg angle, at higher orders of reflection ($n = 2$, 3, etc).

The Bragg equation may be differentiated to give

$$2\Delta d \sin\theta + 2d\cos\theta\Delta\theta = n\Delta\lambda, \tag{5}$$

and dividing equation (5) by equation (4) gives

$$(\Delta d/d) + \cot\theta\Delta\theta = (\Delta\lambda/\lambda). \tag{6}$$

For a chosen set of planes in a perfect crystal, $\Delta d = 0$; and the range of Bragg angles

$$\Delta\theta = (\Delta\lambda/\lambda)\tan\theta, \tag{7}$$

where $\Delta\lambda$ is usually taken to be the full width at half maximum (FWHM) intensity of the x-ray profile. This equation is useful when using characteristic x-radiation and the line width ($\Delta\lambda$) is known.

When using synchrotron radiation which has a continuous spectrum, the formula for the angular range of reflection ($\Delta\omega$) from a perfect crystal is more useful. The formula, derived from the dynamical theory of x-ray diffraction [7], is complicated in the general case but, assuming that absorption is negligible, it takes a particularly simple form in symmetrical diffraction geometries: (see figure 6).

$$\Delta\omega = 2d/\xi. \tag{8}$$

Here, d is, as before, the interplanar spacing and ξ (or sometimes Λ_0) is the extinction length, which is given by the following formula:

$$\xi = \pi V\cos\theta/\lambda r|F|C, \tag{9}$$

where V is the volume of the unit cell, $r = e^2/mc^2 = 2.818$ fm is the classical radius of the electron, F is the structure amplitude (factor) of the reflection (in electron units) and C is the polarization factor. For diamond, the cubic unit cell has volume $V = a^3 = (0.356\,71\text{ nm})^3 = 0.045\text{ nm}^3$.

The polarization factor C is unity for σ-polarization (electric vector perpendicular to the plane of incidence) and $C = |\cos 2\theta|$ for π-polarization (electric vector parallel to the plane of incidence). For unpolarized x-rays emitted from a metal target, $C = (1 + \cos^2 2\theta)/2$. Synchrotron radiation is linearly polarized in the (horizontal) electron orbit plane, so diffraction experiments are usually performed perpendicular to this plane (vertical) in σ-polarization. In π-polarization, the x-ray intensity drops to zero for scattering angles (2θ) close to 90°.

The extinction length gives the depth of crystal that is imaged in an x-ray reflection topograph; rather than the penetration distance $1/\mu$, where μ is the linear absorption coefficient defined in equation (1). If a defect alters the local strain field over a distance comparable to, or greater than, the extinction length, then it will cause image contrast in an x-ray topograph. (See section 6.)

Laue spots are not always as clearly defined as those shown in figure 5, which arise from parallel planes of atoms in the crystal reflecting the x-rays. If however the atoms lie on deformed 'planes' which are not truly planar, then the spots will show streaks: (sometimes called 'asterism'). Furthermore if the crystal has a 'mosaic' structure, comprising several misoriented crystallites, then the Laue spots will appear fragmented. The prevalence of the mosaic structure in Argyle diamonds may account for their high wear resistance in industrial applications, such as polishing. Assuming simple cylindrical bending of lattice 'planes', the radius of curvature r can be calculated from the length of the Laue streak and its deviation from the radial direction. The range of values of r covers many orders of magnitude (from as small as a few millimetres to several kilometres), so a natural logarithmic

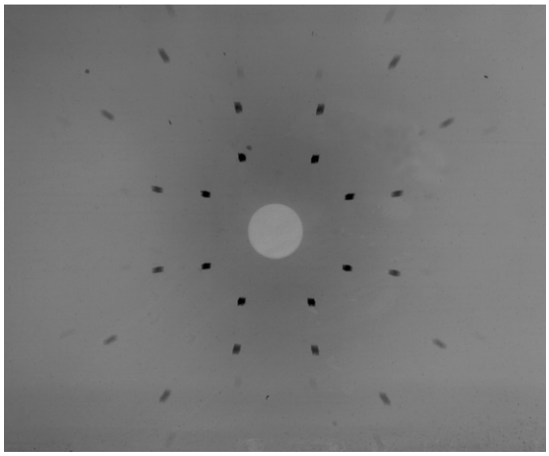

Figure 5. A modern Laue photograph of diamond, taken with white synchrotron radiation, with the incident beam directed along a four-fold (tetrad) symmetry axis.

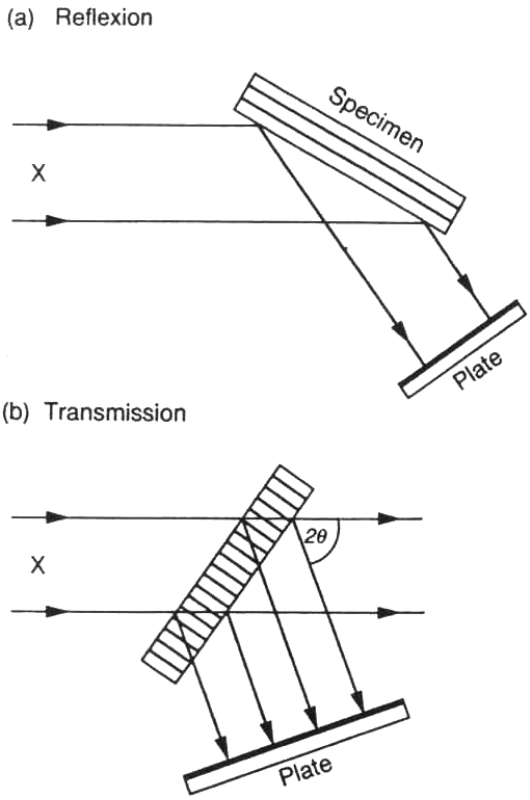

Figure 6. Symmetrical diffraction geometries: (a) symmetrical reflection (Bragg-case); (b) symmetrical transmission (Laue-case). Reproduced with permission from [2]. Copyright 1995, Elsevier.

scale, $\rho = \ln r$, has been proposed as a simple measure of crystalline perfection [8]: the higher the number, the better the perfection. See table 3.

6. X-ray topography

An x-ray topograph is, in effect, a high-resolution Laue spot. It is an image of a single-crystal obtained by one or more Bragg reflections. Contrast on the photographic plate (film) arises from small variations in atomic interplanar spacing, or from misoriented regions (tilts) or from x-ray interference effects [9]. Figure 6 illustrates two commonly used diffraction geometries. For materials which are heavily absorbing, the reflection geometry may be the only option; but information on the plate comes only from a surface layer of thickness comparable to the extinction length (ξ). Transmission techniques are more informative for materials of low absorption, such as diamond, in which the interiors are probed non-destructively—particularly important for gem crystals of great expense!

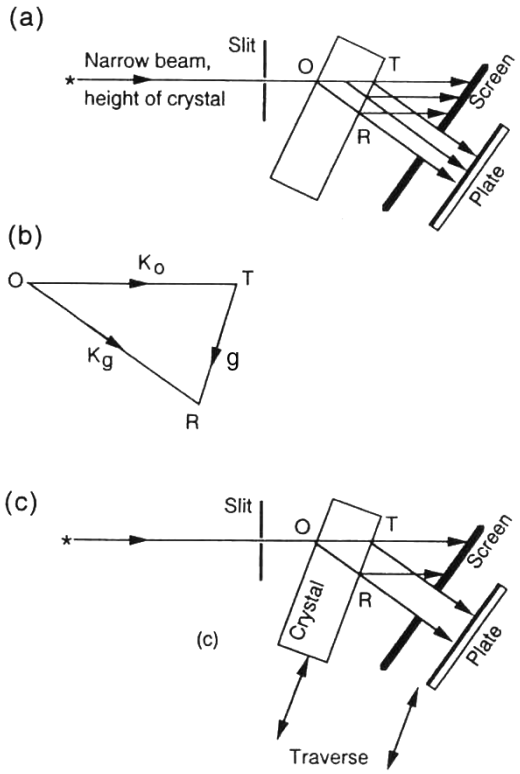

Figure 7. (a) Section topography; (b) wavevector triangle; (c) projection (Lang) topography. Reproduced with permission from [2]. Copyright 1995, Elsevier.

Table 3. Radii of curvature and crystalline perfection. (Note: values of $\rho = \ln r$ are listed for various values of the radius of curvature (r) of cylindrically bent crystals.)

r	1 mm	10 mm	100 mm	1 m	10 m	100 m	1 km
ρ	0	2.3	4.6	6.9	9.2	11.5	13.8

Reflection images of crystal defects were first performed by Berg [10] using parallel-beam characteristic radiation, a technique later improved by Barrett [11] and others, for the imaging of individual dislocations in diffraction (extinction) contrast. The term 'x-ray topograph' was coined by Ramachandran [12], who used continuous (white) radiation to study cleavage plates of diamond in transmission. The reflecting planes were nearly perpendicular to the flat specimen surface; and the specimen and plate were arranged to minimize distortion of the image. The ratio of the distances from the

specimen to (a) the x-ray source and (b) to the photographic plate was 1:12, giving a spatial resolution of 25 μm.

Improvements to the resolution of x-ray topographs (by a factor of 10 or more) have been made by Lang over a number of years [13]. The section topograph [14] uses slit-collimated characteristic x-radiation: see figure 7(a). The slits are carefully chosen so that the crystal selects only the Kα_1 component of the Kα_1–Kα_2 doublet, at the appropriate Bragg angle. This is called 'high-resolution' x-ray topography. The incident x-ray beam is narrow in the (horizontal) plane of the figure but it is as tall as the crystal, so that this beam illuminates a thin section of the crystal. The diffracted beam falls on to a high-resolution photographic plate (such as an Ilford L4 nuclear emulsion), which is held accurately perpendicular to this diffracted beam in order to achieve the best resolution with a thick emulsion. A blurring of the image would be noticeable if the plate were offset by 1°: giving rise to approximately a 1 μm image spread for a 50 μm emulsion thickness and 2 μm for a 100 μm emulsion. The thicker emulsions are used to stop the harder radiations (e.g. Ag Kα_1). An opaque screen (of lead or tantalum) shields the plate from the direct (transmitted) x-ray beam. Using a sealed x-ray tube, running at say 50 kV and 20 mA, exposure times are typically a substantial fraction of an hour to a few hours. For the best resolution, the photographic plate is slowly developed (for about 20 min) at a temperature just above the freezing point of the developer (at about 1 °C); followed by a few minutes in a stop bath, a lengthy period fixing (twice the clearing time) and finally washing in clean water and drying. The whole photographic processing can take an hour or two.

In the diffraction triangle (figure 7(b)), $\boldsymbol{K}_0$ is the wavevector of the incident ray, of magnitude $1/\lambda$; and $\boldsymbol{K}_g$ is that of the diffracted ray of the same magnitude. The third side of this isosceles triangle is the diffraction vector $\boldsymbol{g}$, which is of magnitude $(2\sin\theta)/\lambda$ and direction given by the normal to the Bragg planes. These three vectors satisfy the equation

$$\boldsymbol{K}_g = \boldsymbol{K}_0 + \boldsymbol{g}. \tag{10}$$

In figure 7(a), the triangular prism OTR is called 'the Borrmann triangle' or 'the energy-flow triangle'. Both the transmitted beam $\boldsymbol{K}_0$ and the reflected beam $\boldsymbol{K}_g$ issuing from the exit surface TR, carry information about the defects within OTR. It is usual to record $\boldsymbol{K}_g$ only, but both beams have been imaged for studying stacking-fault fringe patterns [15] and the contrast from dislocations and growth sectors [16].

Projection topography was invented by Lang [17]: often called the 'Lang method'. This also uses slit-collimated characteristic x-rays and it is in effect a superposition of a series of section topographs, achieved by translating the specimen and the photographic plate together, back and forth during the exposure (of several hours), while maintaining the Bragg reflecting condition. See figure 7(c). The apparatus therefore requires an accurate traversing mechanism and it is called a 'Lang camera'. The slit can be opened up, without much loss of resolution, so long as Kα_2 is not reflected as well as Kα_1. The topographic image is an orthographic projection of the crystal, plus its defect content. The full lengths of dislocations are revealed, although their contrast is less than that in section topographs.

Using high-resolution photographic plates, the resolution limit in x-ray topography (XRT) is usually one or two micrometres; so meaningful magnifications from the plates to photographic prints are not more than a few hundred times. Only linear and planar defects can therefore be directly observed; although the combined effect of numerous point defects can be noticed in a greater integrated reflected intensity or a slight change of lattice parameter. X-rays are more penetrating than electrons. Sample thicknesses ranging from hundreds of micrometres to several millimetres are more representative of bulk material than the thin sections required for transmission electron microscopy (TEM).

Examples of section x-ray topographs of natural diamonds are shown in figure 8. These show two different modes of growth for cube-shaped diamonds [18]: cuboid growth on crinkly surfaces of mean orientation {100} and fibrous growth along four ⟨111⟩ directions: as well as compelling evidence that dodecahedral diamonds have dissolved from octahedral crystals to dodecahedra, rather than the dodecahedron being a true growth habit for natural diamond [19]. Octahedral faceted growth is sometimes followed by fibrous growth; and the 'dodecahedral' facets on these so-called 'coated' stones were found to have corrugated surfaces, made up of fine strips of {111}, arising from fibres branching into two ⟨111⟩ directions [20]. Fibrous growth upon a twinned core can give rise to intriguing morphologies [21]. On occasions, the growth sequence is reversed: faceted octahedral growth upon fibrous growth [22]. Using x-ray topography, tetrahedral diamonds have been found to be twins or cleavage fragments [23] and thus not true growth forms; (and diamond definitely belongs to the accepted holosymmetric cubic crystal class $(4/m)\bar{3}(2/m)$ rather than to the hemihedral class $\bar{4}3m$, as is sometimes suggested).

Synthetic diamonds of low nitrogen content (<100 parts per million) may be used as radiation counters in a conduction counting mode; and are especially useful in medical applications. Section x-ray topography was used to show that the diamonds containing many dislocations had lower photocurrents but had the advantage of shorter settling times [24]. When the majority of dislocations were perpendicular to the electric field, higher photocurrents were achieved than when they were parallel to the field.

Two projection topographs are displayed in figure 9. The first is of a large natural octahedral diamond [25]. Here dislocations can be seen as individual black lines (of width about 10 μm) radiating mainly from the central nucleus, but also from other origins; and ending on the crystal surface at locations marked by trigons. Once a subject of huge debate (growth theory *versus* dissolution), trigons are triangular pits displaying the three-fold symmetry of {111} surfaces of diamonds. Some are point bottomed (that is, pyramidal) while others are flat bottomed. All the pyramidal trigons on this diamond were shown to be associated with dislocation outcrops (i.e. they were etch pits); and whereas no dislocations outcropped on flat-bottomed trigons, these trigons could also be associated with dissolution [25].

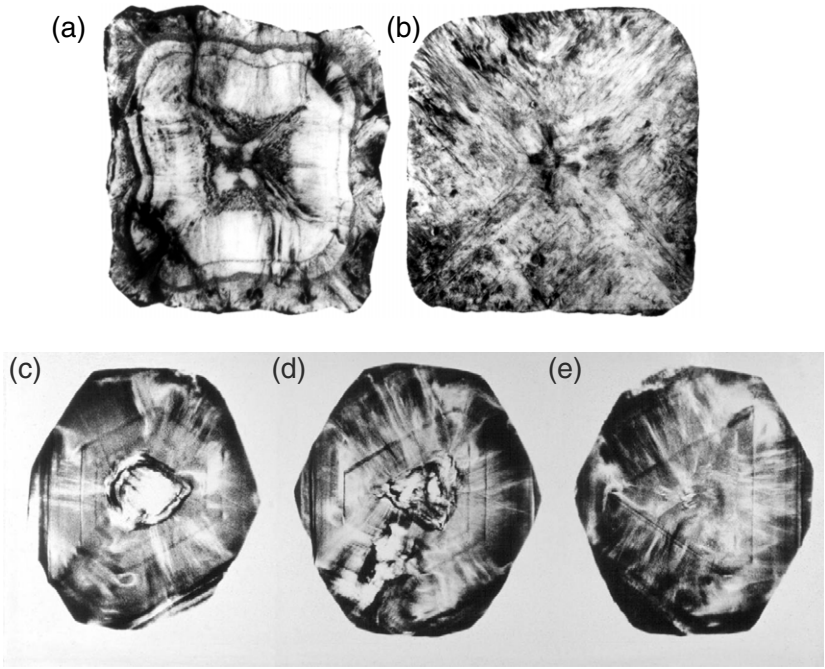

Figure 8. Section x-ray topographs of natural diamonds, all taken with the 440 reflection of Mo Kα_1 radiation. (a) Mid-section of a white cube-shaped diamond showing cuboid growth (on the top of fibrous growth), [001] direction vertical, image width = 1.8 mm reproduced with permission from Taylor & Francis. Originally published in 1972 *Phil. Mag.* **26** 1313–25; (b) mid-section of a brown cube-shaped natural diamond showing fibrous growth throughout, fibre directions parallel to ⟨111⟩, [001] direction vertical, image width = 1.9 mm. Reproduced with permission from Taylor & Francis. Originally published in 1972 *Phil. Mag.* **26** 1313–25. (c)–(e) A series of three section topographs, taken at 0.25 mm separations, of a terraced dodecahedral diamond, showing sections of internal octahedral growth surfaces, [1$\bar{1}$0] direction vertical, image width = 1.7 mm, reprinted from [19], copyright 1974, with permission from Elsevier.

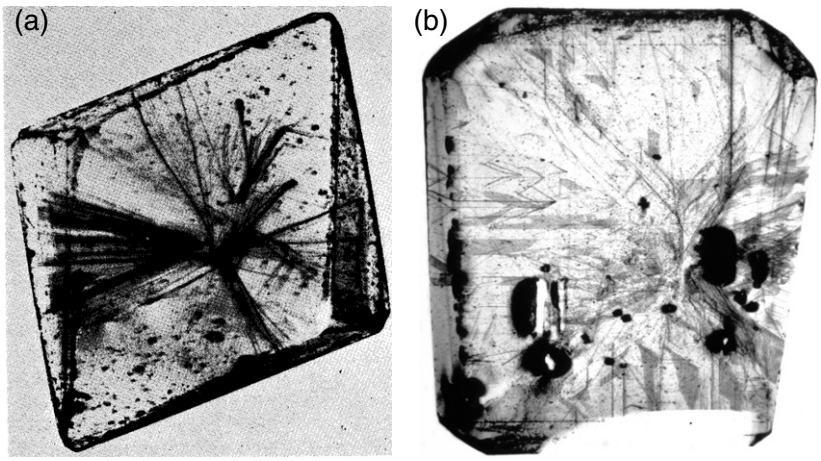

Figure 9. Projection topographs revealing dislocations, taken with the 111 reflection of Mo Kα_1 radiation. (a) Natural octahedral diamond, edge length 5.2 mm, topograph taken by A R Lang [25] reprinted with permission of Oxford University Press (figure 35, page 85). (b) Slice cut from an octahedral synthetic diamond, image width 4 mm [26].

Figure 9(b) displays a projection topograph of a slice (0.7 mm thick) of a synthetic octahedral diamond [26], grown (*circa* 1988) by the reconstitution technique. Here dislocations can also be seen as dark lines; as well as stacking faults as grey triangular areas, and large metal inclusions (light) together with their associated strain fields (dark).

Another Lang invention is the limited projection topograph [25], in which the specimen and photographic plate are again traversed together. The slit in the opaque screen between the crystal and the photographic plate is closed down in order to eliminate unwanted x-rays coming, for example, from regions exhibiting severe surface damage, which would otherwise obscure seeing the more perfect interior. See figure 10(a). Alternatively, the exit surface of the crystal may be of prime interest, in which case the arrangement in figure 10(b) would be chosen. One does not want the direct beam to strike the photographic plate, but a 'bright field' projection topograph may be recorded in the geometry of figure 10(c).

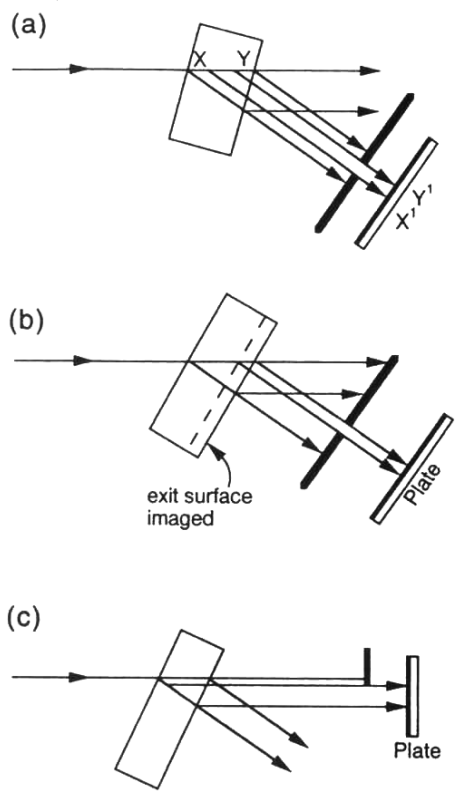

Figure 10. Limited projection topography (a) imaging the interior of a crystal without the surface damage; (b) imaging just the exit surface; (c) imaging with the transmitted beam (bright field). Reproduced with permission from [2]. Copyright 1995, Elsevier.

In order to recover three-dimensional information, stereoscopic pairs of images may be recorded and viewed together, either observing photographic prints with a stereo-viewer or examining the topographic plates with left and right eyes looking through separate (monocular) microscopes. One technique is to image the hkl and $\bar{h}\bar{k}\bar{l}$ reflections [17]. Another technique is to image the same Bragg reflection but the crystal is rotated a few degrees about the Bragg-plane normal (that is, about the $\boldsymbol{g}$-vector) between taking the two topographs [27, 28]. The latter technique has the advantage of being able to vary the effective stereoscopic angle: (15° being a favourite choice). In a comparison of the perfection of synthetic diamond with that of natural diamond, stereoscopic pairs of topographs were taken in order to examine the dislocations, growth-sector boundaries, stacking faults and their associated strains [29].

With highly collimated synchrotron x-radiation, the necessity for traversing the specimen and photographic plate is removed. The entire crystal may be illuminated with a wide beam of x-rays at the appropriate Bragg angle and the topograph recorded without scanning, giving a consequent shortening of the exposure time. Furthermore, the freedom to choose a wavelength from the continuum emitted by a synchrotron is a huge advantage over the limited choice of characteristic lines available from common metal targets. One can do very simple experiments or highly sophisticated ones. For example, a crystal illuminated with white x-radiation will select an appropriate wavelength (λ) from the continuum and diffract: the crystal does not need to be accurately oriented. With such a wide range of wavelengths available, the experimenter may wonder which wavelength to choose: perhaps an advantageous diffraction geometry in which the incident x-rays are directed precisely along a chosen crystallographic direction. Consideration of the harmonics ($\lambda/2$, $\lambda/3$, $\lambda/4$, etc), which also satisfy Bragg's law, may however be needed in the analysis. In the case of diamond, the 222 'forbidden' reflection is very weak; so if the diamond is set for the 111 reflection, the $\lambda/2$ harmonic gives very little effect on the diffraction image. The wavelength dependence (0.05–0.25 nm) of x-ray diffraction contrast from various defects in a slice of natural diamond is discussed in [30].

An example of the use of continuous synchrotron radiation for section x-ray topography is given in figure 11. This shows a natural diamond twin: a pair of interpenetrant cubes [31]. A slit was arranged to illuminate just the mid-section and many images were recorded simultaneously on the same photographic plate. Some of these came from one member of the twin, some from the other and some from both [32]. The images in figures 11(b) and (c) show the two members of the twin separately, without damaging the crystal. Immediately apparent from these topographs is the fibrous internal structure, common in coloured cube-shaped diamonds: (compare with figure 8(b)).

7. Defects in crystals

Defects in crystals may be classified by their dimensions: 0, 1, 2 or 3. Point defects (of zero dimension) include vacancies

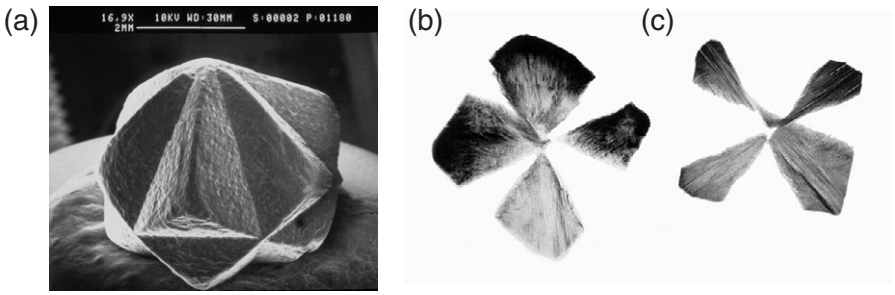

Figure 11. Natural diamond twin. (a) Scanning electron microscope image, scale mark = 2 mm; (b) synchrotron mid-section topograph imaging one member of the twin, 331 reflection, image diameter 2.2 mm; (c) simultaneous topograph imaging the other member of the twin, 004 reflection. Reproduced with the permission of the International Union of Crystallography from [31].

(an atom missing from the structure), interstitial atoms, substitutional impurities and Frenkel defects (a vacancy–interstitial pair). They are too small to be seen by x-ray topography!

Linear defects are called dislocations, which may be either of edge, screw or mixed types. They are characterized by their Burgers vectors. Taking equal numbers of steps between atoms to the right, downwards, to the left and upwards would create a closed loop in a perfect crystal structure. If however such a Burgers circuit were made around a dislocation, the finish point (F) and the start point (S) will not coincide. The 'closure failure' (FS) is the Burgers vector ($\boldsymbol{b}$) of the dislocation. Representing the direction of the dislocation line by the vector $\boldsymbol{l}$; $\boldsymbol{b}$ and $\boldsymbol{l}$ are perpendicular in edge dislocations, they are parallel in screw dislocations and they are at an inclined angle in mixed dislocations. In diamond, dislocation lines may have various directions, but the most common Burgers vector is $\frac{1}{2}$[110].

Dislocations create strain fields extending over many micrometres, comparable to the extinction length, and can therefore be imaged in x-ray topography. The upper limit for dislocation density that can be easily seen in XRT is approximately 10^4 mm^{-2}; so XRT nicely complements transmission electron microscopy, as this figure is the lower limit of the dislocation density that can be conveniently imaged in TEM.

The direction of the Burgers vector may be determined from x-ray topography by the use of the so-called '$\boldsymbol{g}\cdot\boldsymbol{b}=0$' criterion, where $\boldsymbol{g}$ is the diffraction vector. Displacements perpendicular to the diffraction vector do not affect the phase of the diffracted x-ray beam and are therefore invisible. The procedure requires the visibility of the dislocation in one topograph ($\boldsymbol{g}_0\cdot\boldsymbol{b}\neq 0$) but invisibility in another two with differing diffraction vectors: $\boldsymbol{g}_1\cdot\boldsymbol{b}=0$ and $\boldsymbol{g}_2\cdot\boldsymbol{b}=0$. Each of these two equations defines a plane in which $\boldsymbol{b}$ must lie, and their intersection gives the direction of $\boldsymbol{b}$. This procedure works perfectly for screw dislocations, for which the surrounding strain $\boldsymbol{u}$ is parallel to $\boldsymbol{b}$; and it works approximately for other types of dislocation. The strain field of an edge dislocation also has a component parallel to $\boldsymbol{b}\times\boldsymbol{l}$, and so for complete invisibility, the additional criterion $\boldsymbol{g}\cdot(\boldsymbol{b}\times\boldsymbol{l})=0$ should also be applied. The strain field $\boldsymbol{u}$ of a mixed dislocation has components in all three mutually perpendicular directions ($\boldsymbol{b}$, $\boldsymbol{b}\times\boldsymbol{l}$ and $\boldsymbol{l}\times\boldsymbol{b}\times\boldsymbol{l}$) and so is never completely invisible in any x-ray topograph; but the components of $\boldsymbol{u}$ in the latter two directions are usually much smaller than that in the first, and so the '$\boldsymbol{g}\cdot\boldsymbol{b}=0$' criterion approximately applies in all cases. The direct image width of a dislocation in a transmission x-ray topograph can be estimated as approximately $(\xi/2\pi)\boldsymbol{g}\cdot\boldsymbol{b}$.

Two-dimensional (planar) defects include twin boundaries, stacking faults and the platelets found in natural diamonds. The face-centred cubic structure may be considered as the stacking of layers of spherical atoms in hexagonal arrays, each layer sitting in the gaps of the previous layer, with a stacking sequence ABCABCABC$\cdots$ A simple example of a twin would be the sequence ABCABCBACBA$\cdots$: what comes after the middle C is reflected in what came before. And an example of a stacking fault would be ABCABCBCABCABC$\cdots$

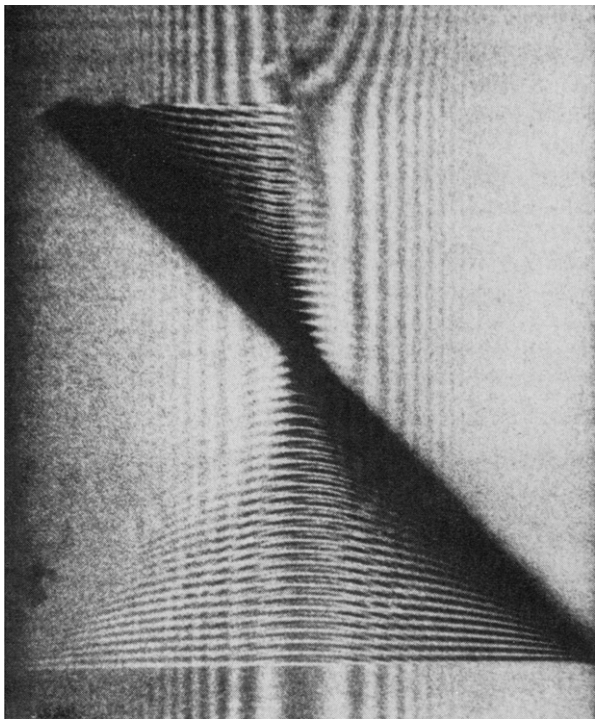

Figure 12. Section topograph of a stacking fault in diamond, 111 reflection, 0.15 nm synchrotron x-radiation, pure π-polarization mode, image width 0.7 mm. Reproduced with the permission of the International Union of Crystallography from [34].

in which material either side of the stacking fault has the same stacking sequence (cyclic-ABC). The fault vectors $\boldsymbol{f}$ of stacking faults may also be determined by x-ray topography, using the criterion for invisibility $\boldsymbol{g}\cdot\boldsymbol{f}=m$, where m is an integer. In crystals with the diamond structure, $\boldsymbol{f}$ is either $\frac{1}{3}$[111] for an intrinsic type of stacking fault or $\frac{2}{3}$[111] for the theoretically possible extrinsic stacking fault [33].

Stacking faults may cause beautiful x-ray interference effects in x-ray topographs. See figure 12. In a polished parallelepiped specimen of natural diamond ($5\times 2\times 1$ mm^3), fringe patterns were caused by a single intrinsic stacking fault of area 1.3 mm^2. These patterns were recorded using synchrotron radiation in pure σ and pure π polarization, as well as in mixed polarization, which aided their interpretation by computer simulation [34].

8. Spike topography

Whatever the composition or structure of platelets in natural diamond may be (interstitial carbon, possibly with some nitrogen), their average radius may be estimated by the non-destructive technique of spike topography [35]. These planar defects, of only a few atoms thick, lie on {100} planes. They are roughly circular or elliptical, but sometimes elongated along ⟨110⟩ directions; and they are typically 10–100 nm in diameter: that is, one or two orders of magnitude smaller than the resolution limit of conventional x-ray topography (1 μm). Let us say that they are extended in the $\pm Ox$ and $\pm Oy$ directions, but thin in the $\pm Oz$ direction. In diffraction, lengths become

reciprocal lengths, so a platelet becomes small in the $\pm Ox$ and $\pm Oy$ directions but extended in the $\pm Oz$ direction: that is, it becomes cigar-shaped or a 'spike'. These produce the so-called 'extra reflections' seen in Laue photographs [36] of type Ia diamonds. For a review, see [37].

In spike topography, the crystal is deliberately offset a degree or so from the exact Bragg reflecting angle [25, 38]. One may imagine the Ewald sphere intersecting one or more spikes surrounding a Laue spot, but missing the reciprocal lattice point itself. The intensity of the diffracted beam is thus very low (being inversely proportional to the square of the offset angle) and exposures are long: several days with a sealed tube [35], several hours with a rotating-anode generator, even 20 min or more with monochromatic synchrotron radiation from a wiggler [39]. In regions of crystal devoid of platelets, the spike topograph records nothing (apart from some background x-ray scattering). Therefore the presence of platelets can be mapped in such a topograph; and in addition their average radius can be estimated [35, 38, 40] from measurements of the inter-quartile width of the spike profile. The IQW is defined as the width between the positions on the profile at one quarter and three quarters of the maximum height. It is a practicable parameter because it is independent of the overall blackness of the topographic image, which would vary according to x-ray intensity, exposure time and development conditions.

The shape of the optical density profile of a spike topograph arises from the convolution of two functions: the platelet number density and the Airy diffraction intensity profile appropriate for a mean radius of platelets behaving as an assembly of circular apertures. At the edges of the diamond, or at an artificially introduced edge caused by the shadow of a tantalum screen, the platelet number density is a step function: zero outside and taking a positive value inside. This convolution is thus a simple integration of the Airy profile, and this can be recorded by taking a microdensitometer traverse across the topograph. The mean platelet radius R is given by

$$R = M\lambda L/2\pi W \tag{11}$$

where λ is the wavelength of the x-rays used, L is the specimen-to-plate distance, W is the measured IQW minus one-half of the microdensitometer slit width, and M is a dimensionless constant, taking the value 1.817 (for a single integration, appropriate for a narrow microdensitometer slit or for a thin crystal) or 2.022 (for the double integration for a wide slit or for a thick crystal) [40]. These two constants are so similar that the experimenter need not worry too much about the microdensitometry precisely fulfilling the single or double integration conditions.

Transmission electron microscopy gives wonderful images of platelets [41] in thin sections of natural diamond, but the technique is necessarily destructive. When mapping is not required but just an estimate of average platelet radius, then infrared spectroscopy may be used as an alternative non-destructive technique. The frequency of the B′ (platelet) peak has been found to vary inversely with platelet radius [42]. Over the wavelength range 7.29–7.35 μm, an empirical formula has been suggested relating the platelet radius R measured in angstroms with the wavelength λ of the B′ peak in μm:

$$R = 5748\lambda - 41\,846. \tag{12}$$

9. Double-crystal x-ray topography

Double-crystal topography employs Bragg reflections from two crystals: first from a perfect (reference, or monochromating) crystal and then from the specimen. For a review, see [43]. The reference crystals must be free of defects, or these too will be imaged on the x-ray topograph. Commercially available single-crystals of silicon, germanium and quartz are very suitable. They Bragg reflect x-rays only over a very small range of incident angles and they do so with high efficiency: so that many Bragg reflections can be used without significant loss of intensity. The sensitivity to lattice parameter variations, or interplanar variations $\Delta d/d$, in single-crystal x-ray topography may be as good as 10^{-4}, but this figure is greatly improved to 10^{-7}–10^{-8} in double-crystal topographs.

The so-called (+, −) non-dispersive diffraction geometry is favoured as the x-rays, diffracted first to the left and secondly to the right, emerge parallel (or almost so) to the incident beam. The doubly-reflected intensity, recorded as one crystal is slowly rotated, is called the 'rocking curve'. If the two Bragg angles are the same (or nearly so) then the rocking curve can be very narrow: typically a few seconds of arc. The sides (or 'flanks') of the rocking curve can therefore be very steep; and if a topograph be taken while the relative setting of the crystals is halfway up a 'flank', then very small variations in local Bragg angle are imaged as large variations in intensity on the photographic plate [44]. These small, reproducible, changes in angle set very high engineering standards for the equipment.

With Cu Kα_1 radiation, there are only five distinct reflections from diamond: 111, 220, 311, 400 and 331. The best choice of reference crystal for the diamond-111 reflection would be the 220 reflection from a (110) surface of germanium [26]. The Bragg angles are nearly equal, being 21.965° and 22.648°, respectively. Possible choices of reference crystals and orientations for the other reflections are given in a useful table [26].

There have been many studies of diamond employing double-crystal topographic techniques, using either characteristic or synchrotron radiation. Natural diamonds are sometimes found which are half white and half brown, with more nitrogen in the white regions than in the brown: (1.6 times). Nitrogen is often clustered into A-defects (two nitrogen atoms) or B-defects (four nitrogen atoms surrounding a vacancy). Using a combination of x-ray topographic and other techniques, the brown regions were found to be significantly more distorted than the white (by a factor of 4). Assuming that the two halves of each stone had suffered the same histories of pressure, temperature and environment; the conclusion was that the nitrogen (in A and B forms) had stiffened the diamond structure against plastic deformation [45].

Synthetic diamonds grown by the high-pressure high-temperature (HP/HT) technique, when grown in the [111] direction, sometimes contain 'clouds' of opaque particles of

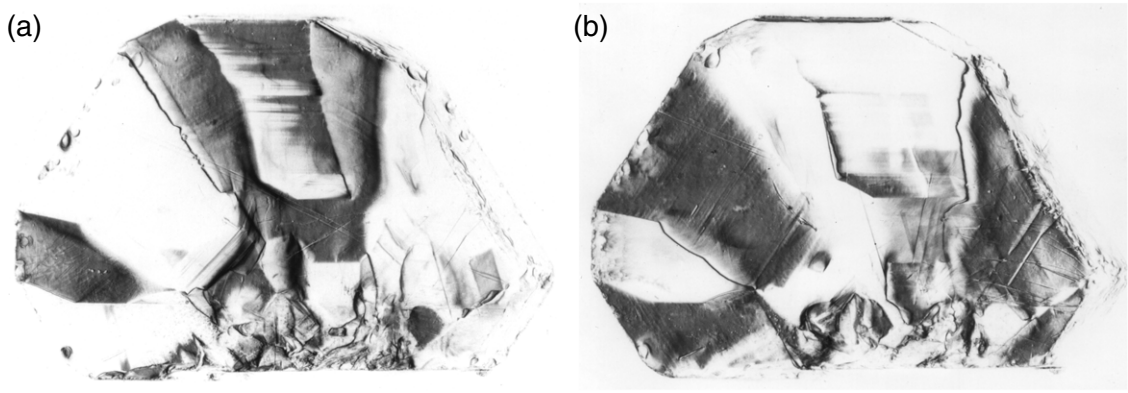

Figure 13. Two double-crystal x-ray topographs (from a long sequence) of a synthetic diamond. Silicon-175 reflexion + diamond-440 reflection, $\theta = 64°$, $\lambda = 0.113$ nm, image width = 5 mm. (a) (110) growth sector reflecting, showing as a dark region on left-hand side of image; (b) adjacent (111) growth sector reflecting, upper-left. Angular separation between (a) and (b) = 3 arcsecond (14.5 μrad). Reprinted from [47]. Copyright 1991, The Royal Society.

diameter 0.25–5.0 μm: (so-called 'pin-point' inclusions). The influence of these inclusions upon both the lattice parameter and the lattice tilting of growth sectors [46] has been investigated by the four-azimuth technique [26, 47]. Here the silicon-800 reflection selected 0.096 nm synchrotron radiation at a Bragg angle θ of 45° and this matched the diamond-333 reflection rather well at $\theta = 44.42°$. (The $\lambda/2$ harmonic was virtually absent as the diamond-666 reflection is 'forbidden'.) Small regions of crystal were probed using a 100 μm XY-translatable pin-hole positioned between the silicon monochromator and the diamond specimen. A radiograph and a rocking curve were recorded at each position; and thus the whole crystal was mapped point by point. Values of rocking curve widths were in the range of 4–20 arcseconds and compared with the theoretical value for perfect diamond of 3.5 arcseconds in this diffraction geometry. Both lattice parameter variation and relative misorientation (tilt) affect the rocking curve width. These two effects can be separated by taking four sequences of topographs with the specimen turned through intervals of 90° about the Bragg-plane normal (g-vector): $\chi = 0°$, 90°, 180° and 270°. Tilts of up to 12.5 arcseconds were recorded in areas populated by 'pin-point' inclusions.

A similar four-azimuth study was made of growth-sector boundaries, lattice bending and axisymmetric strain surrounding cylindrical metal (Fe–Ni) inclusions, elongated along a ⟨110⟩ direction, within HP/HT diamonds grown in the [100] direction [48]. Lattice parameter variations $\Delta d/d$ for (100) planes were measured in the range 7–36 parts per million. Lattice bending (5 arcsecond) was found in the minor {113} and {110} growth sectors, caused by compressive stresses from the major {001} and {111} sectors.

An exhaustive study of lattice parameter variations caused by substitutional nitrogen in a large (5.0×3.2 mm^2) synthetic type Ib diamond was made using synchrotron radiation [47]. The silicon-175 asymmetric reflection was matched with the diamond-440 symmetric reflection. Sequences of double-crystal topographs at high Bragg angles ($\theta = 64°$, $\lambda = 0.113$ nm; and $\theta = 75°$, $\lambda = 0.121$ nm) imaged the growth sectors in turn, as the specimen was accurately rocked in

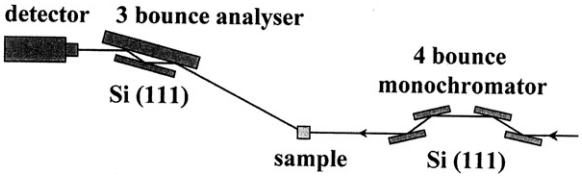

Figure 14. Multi-crystal arrangement for measuring strain and for recording reciprocal-space maps [49].

1 arcsecond steps through the Bragg reflecting condition for each sector. Two x-ray topographs taken (from the very large number actually recorded) are shown in figure 13. A (110) growth sector contained very little nitrogen (concentration < 1 part per million), whereas a (111) sector contained 88 ± 7 parts per million nitrogen and had a greater relative lattice parameter $\Delta a/a = 11.8 \pm 0.7$ parts per million. To be able to map lattice parameter differences, with better than parts per million accuracy, across many millimetres of crystal is a remarkable achievement.

10. Triple-crystal techniques—reciprocal-space mapping

The effects of variations in lattice parameter and lattice tilting can readily be separated if a third crystal is used to analyse the beam diffracted from the specimen. In practice, 'triple-crystal' techniques involve more than three crystals and are perhaps better known as 'triple-axis' techniques. This, however, can also be misleading, as each of the three components (monochromator, specimen and analyser) may be adjusted about several different axes. A typical multi-crystal arrangement is shown in figure 14. Here the monochromator involves four Bragg reflections and the analyser has three. The beam incident upon the specimen is thus well conditioned; and the detector is not directed towards the beams incident upon, or diffracted from, the specimen, with a consequent excellent signal-to-noise ratio. For a review of triple-axis techniques, see [43].

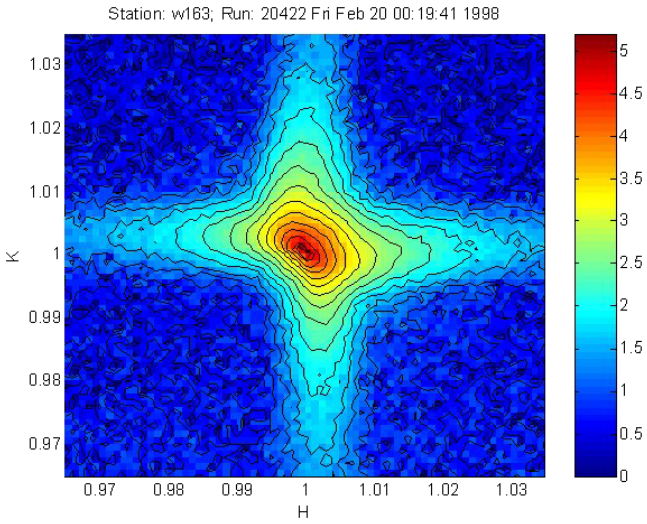

Figure 15. High-resolution reciprocal-space map of the 111 reflection in a natural type Ia diamond. The coloured bar is a logarithmic scale (base 10) of intensity. Reproduced with permission from [51]. Copyright 1999, IOP Publishing Ltd.

Reciprocal-space mapping is a technique complementary to x-ray topography in that it can give diffraction information in all directions at a selected point in the crystal; whereas x-ray topography enables a relatively large volume of crystal to be imaged by a single diffraction vector. The specimen is mounted on a φ-axis riding on a χ-circle which rotates about the ω-axis. The diffracted beam enters the detector via the analyser, which turns about the 2θ-axis. Small angular ranges are transformed into reciprocal-space coordinates by the following equations [50]:

$$\begin{aligned}\Delta g_x &= (1/\lambda)\{\cos[2\theta-\omega](\Delta 2\theta-\Delta\omega)+\cos\omega\Delta\omega\}\\ \Delta g_y &= (1/\lambda)\{\sin[2\theta-\omega](\Delta 2\theta-\Delta\omega)-\sin\omega\Delta\omega\}.\end{aligned} \tag{13}$$

Reciprocal-space maps can therefore be computed from the angular data; and conversely, length scales can be obtained from features in a reciprocal-space map by substituting the relevant angular decrements into these equations. When the diffraction vector $\boldsymbol{g}$ lies in the plane of the reciprocal-space map, x-ray intensity spreading in the direction of $\boldsymbol{g}$ comes from lattice parameter variations, while intensity spreading at right angles to $\boldsymbol{g}$ arises from lattice tilting. Measurements made by this technique [51] of lattice bending in synthetic diamonds (in the angular range of 40–100 arcsecond) confirmed those made by double-crystal topography [48]; and measurements of lattice strain in various growth sectors of another synthetic diamond were in the range of 6.8×10^{-6}–7.8×10^{-6}, which is typical of HP/HT diamonds.

Platelets in natural diamonds have already been mentioned in section 8. High-resolution reciprocal-space maps surrounding chosen Bragg reflections have been made [51], an example of which is shown in figure 15. Here the 'spikes' in four of the six ⟨100⟩ directions surrounding the 111 reciprocal lattice point are clearly seen in this [100]–[010] plane. From the widths of the spikes, estimates can be made of the average platelet diameter, which is here 27.8 ± 3.4 nm.

Reciprocal space may be mapped in all three dimensions to study the shapes and sizes (0.2–1.6 μm) of individual crystallites (grains) in polycrystalline chemical vapour deposited (CVD) diamond, together with measurements of lattice parameter and microstrain [52]. The third adjustable parameter, in addition to ω and 2θ, is the azimuthal angle χ. Bragg reflections from each grain were isolated in reciprocal space by reducing the divergence of the x-ray beam by the introduction of suitable slits. Lattice parameter values were measured in the range 0.356 46–0.356 66 nm, with an accuracy of $\pm0.000\,01$ nm.

11. Scanning x-ray microscopy

Conventional radiography uses an x-ray area detector, or film, and bathes the whole sample in a wide x-ray beam: see section 3 above. The image resolution is then given by the spatial resolution of the detector. Instead, a collimator of small cross-section can be used to produce a fine incident x-ray beam and the intensity of the beam transmitted through the sample may be measured by means of an x-ray photon counting detector, such as a scintillation counter or a cooled germanium solid-state detector. The spatial resolution is then determined by the nanocollimator size and any slight

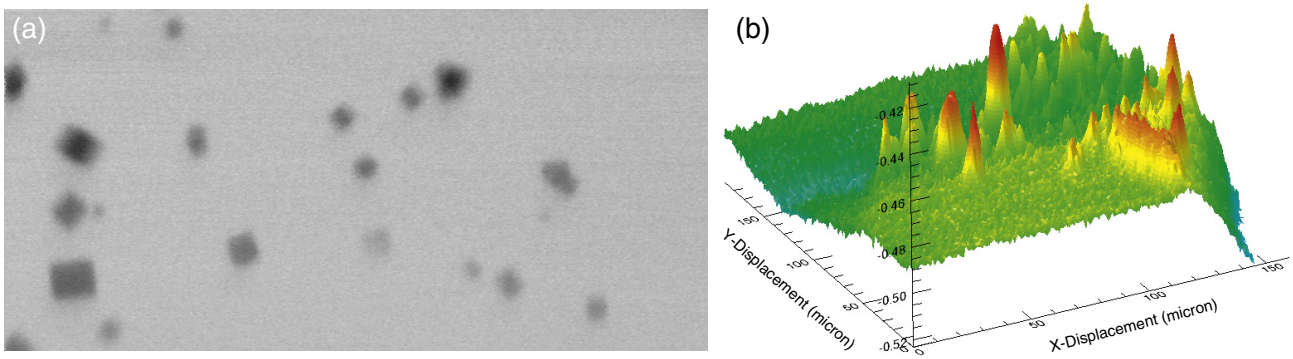

Figure 16. Scanning x-ray micrographs taken at Beamline B16 of the Diamond Light Source. Collimator dimensions approx 1 μm × 1 μm, scanning step size = 0.5 μm. (a) Part of a synthetic diamond. The field of view is 140 μm wide by 70 μm high, taken with monochromatic x-radiation, energy = 12.4 keV (wavelength = 1.0 Å). (b) A monochromatic (15 keV) radiograph of metal inclusions in a synthetic diamond grit particle. The X- and Y-axes are graduated from 0 to 150 μm and the Z-axis is proportional to x-ray absorption contrast.

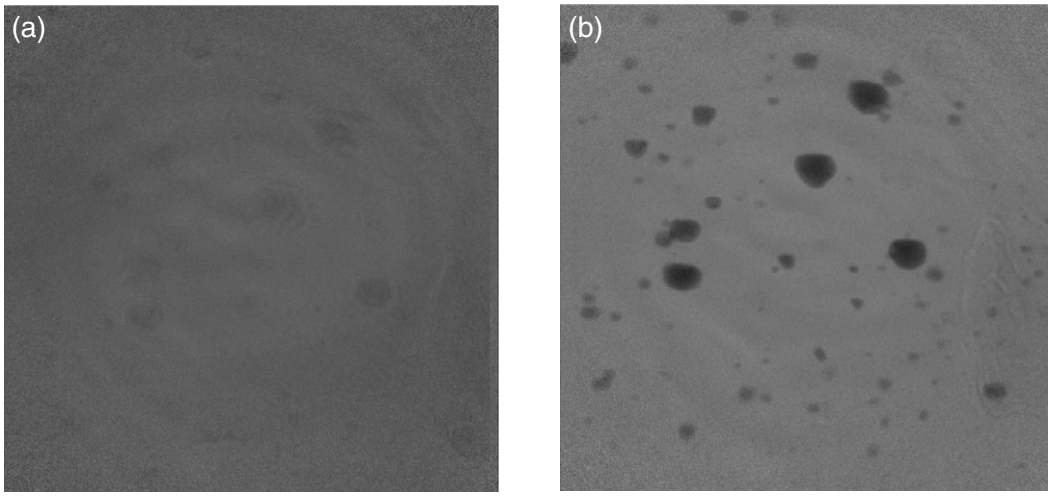

Figure 17. Images (30 μm × 30 μm) of part of a diamond grit particle, taken (a) below and (b) above the Fe K-absorption edge = 7.112 keV. (a) Taken at 7.05 keV; (b) taken at 7.20 keV. Pictures by Joy Andrews Hayter at Stanford Synchrotron Radiation Lightsource.

divergence. This technique requires translation of the sample (e.g. on a piezoelectric X–Y scanning stage) so as to scan the x-ray beam across objects of interest within the specimen and to build up a picture, pixel by pixel. The use of a photon counting detector ensures high x-ray detection efficiency. By suitable positioning of the detector, such a scanning x-ray microscope may also be used in other modes of operation: x-ray diffraction, x-ray fluorescence and small-angle scattering. Specimens may be viewed not only in normal incidence, but also as stereo-pairs or in grazing-incidence reflection-geometry.

The intrinsic low divergence of nanocollimators gives a relatively long working distance, and allows thick samples and embedded specimens to be examined: samples that cannot easily be studied using micro-focussing techniques (such as capillary optics and zone plates), which have larger x-ray beam divergences. Furthermore, x-ray focusing optics are wavelength-dependent; whereas a collimator transmits all wavelengths, which may be analysed in an energy-sensitive detector for localized spectroscopy.

Collimators have been successfully made [53] with cross-sections of only 300 nm × 500 nm and of high aspect ratios for use with hard x-rays of energies up to 30 keV (wavelength λ = 0.041 nm). The method involves planar (two-dimensional) nano-fabrication using a direct-write electron-beam 'lift-off' technique [54]. For example, a collimator of aspect ratio 5000 gives a divergence of 0.2 mrad. This allows the x-ray beam size to be maintained over a longer distance (∼2.5 mm for a 0.5 μm aperture) and therefore makes it ideal for the study of the thicker specimens or embedded samples. The low divergence is also advantageous for diffraction experiments. It should be noted that diffraction from the aperture itself gives an angular divergence (in radians) given by $\lambda/(2d)$. For 1 Å (0.1 nm) radiation, a nanocollimator with d = 0.5 μm will have its angular divergence broadened by 0.1 mrad by diffraction. This is still less than the intrinsic collimator divergence.

The Test Beamline B16 at the Diamond Light Source (DLS) is ideal for trying out new experiments and novel x-ray optics and detectors. The DLS has an energy of 3 GeV, a highly stable current of 300 mA and a very small emittance of 2.7 nm radians. It should be noted that B16 is not the brightest source available, as the radiation comes from a bending magnet rather than an insertion device (wiggler or undulator). An example of a scanning x-ray micrograph is given in figure 16(a), showing a part of a slice (0.5 mm thick) of synthetic diamond containing metal inclusions. This micrograph was taken with monochromatic x-radiation of energy 12.4 keV (λ = 0.1 nm). The collimator dimensions were approximately 1 μm × 1 μm and the scanning step length was 0.5 μm. The field of view is 140 μm wide by 70 μm high. Some metal inclusions appear to be square. An alternative representation of images is shown in figure 16(b). This shows part (150 μm × 150 μm) of a diamond grit particle containing metal inclusions. Absorption is measured vertically in this display.

Monochromatic synchrotron radiation may be used to probe specimens at energies above and below chosen x-ray absorption edges for element-specific contrast. The example in figure 17 shows metal inclusions in a diamond grit particle, taken with the transmission x-ray microscope at the Stanford Synchrotron Radiation Lightsource (SSRL). The inclusions were studied with radiations below and above the iron, cobalt and nickel K-absorption edges. In the latter two cases (Co and Ni), there was little difference in the contrast, but with Fe the contrast is very different. The conclusion is that these particular inclusions are composed mainly of iron.

Early experiments (1990s) at the Daresbury synchrotron gave very small fluxes of monochromatic radiation through collimators of square micrometre dimensions: at Station 7.6, about 1 photon s^{-1}. At the Diamond Light Source, a few hundred counts per second are typical. By combining this collimator with refractive lens optics (8 keV) at Station ID06 of the European Synchrotron Radiation Facility (ESRF), 400 000 counts per second pass through! The lens system is a linear array of 17 beryllium parabolic concave lenses with a total focal length of 3 m, which matches well with the divergence of the collimator. Clearly scanning x-ray microscopy has a bright future!

12. Conclusion

X-rays possess major advantages over electron beams in some applications. First, no vacuum is required. Secondly, there are no charging effects. Thirdly, x-rays penetrate further into materials than electrons. The removal of such constraints enables studies to be made of electrical insulators, such as diamond; as well as performing localized spectroscopy of selected regions within the interiors of specimens, beyond the reach of electrons. Synchrotron radiation has many useful properties, including the ability to tune the energy of the incident beam to absorption edges of chosen elements.

Acknowledgments

I would like to dedicate this review to the memory of Professor Andrew Lang, FRS (1924–2008) of the University of Bristol, who did so much pioneering work in x-ray topography and diamond physics. For financial and other assistance, I thank De Beers Industrial Diamond Division Pty Ltd, Element Six Ltd, the Engineering and Physical Science Research Council (EPSRC); and the Director and Staff of the CLRC Daresbury Laboratory (DL), the Diamond Light Source (DLS), the European Synchrotron Radiation Facility (ESRF) and the Stanford Synchrotron Research Lightsource (SSRL). I thank the following colleagues and research students at Royal Holloway University of London (RHUL) and others for discussions and help with experiments: James Allerton (RHUL), Stephen Clackson (RHUL), Igor Dolbnya (DLS), Mina Golshan (DL/RHUL), Joy Andrews Hayter (SSRL), Grzegorz Kowalski (RHUL), Andrew Lang (Bristol), David Laundy (DL), Walmir Machado (RHUL), Tony Makepeace (Bristol), Stuart Nailer (RHUL), Victor Petrashov (RHUL), Kawal Sawhney (DLS), Rais Shaikhaidarov (RHUL), Anatoly Snigirev (ESRF), Richard Waggett (RHUL), Wojciech Wierzchowski (RHUL) and Andrew Yacoot (RHUL).

References

[1] Margaritondo G 2002 *Elements of Synchrotron Light* (Oxford: Oxford University Press)
[2] Moore M 1995 Synchrotron x-ray topography *Radiat. Phys. Chem.* **45** 427–44
[3] Wilson A J C and Prince E (ed) 1999 *International Tables for Crystallography* vol C (Dordrecht: Kluwer) p 230 published for the International Union of Crystallography
[4] Peele A G and Nugent K A 2008 Physical optics basis for the x-ray phase imaging of low contrast samples: a primer *Crystallogr. Rev.* **14** 263–90
[5] Kowalski G, Moore M and Nailer S G 1999 Application of x-ray phase-contrast imaging to polycrystalline CVD diamond *J. Phys. D: Appl. Phys.* **32** A166–71
[6] Bragg W H and Bragg W L 1913 The structure of the diamond *Nature* **91** 557 (only)
Bragg W H and Bragg W L 1914 The structure of the diamond *Proc. R. Soc.* A **89** 277–91
[7] Authier A 2001 *Dynamical Theory of X-Ray Diffraction* (*IUCr Monograph on Crystallography* vol 11) (Oxford: Oxford University Press)
[8] Clackson S G and Moore M 1992 An x-ray study of some Argyle diamonds *Indust. Diamond Rev.* **52** 192–4
[9] Lang A R 1970 Recent applications of x-ray topography *Modern Diffraction and Imaging Techniques* ed S Amelinckx, R Gevers, G Remaut and I vanLanduyt (Amsterdam: North-Holland) pp 407–79
[10] Berg W F 1931 Examination of the lattice disturbances in crystals *Naturwissenschaften* **19** 391–6 (in German)
[11] Barrett C S 1945 A new microscopy and its potentialities *Trans. AIME* **161** 15–64
[12] Ramachandran G N 1944 x-ray topographs of diamond *Proc. Indian Acad. Sci* A **19** 280–92
[13] Lang A R 1993 The early days of high-resolution x-ray topography *J. Phys. D: Appl. Phys.* **26** A1–8
[14] Lang A R 1957 A method for the examination of crystal sections using penetrating characteristic x-radiation *Acta Metall.* **5** 358–64
[15] Jiang S-S and Lang A R 1983 Stacking fault contrast in x-ray diffraction: a high-resolution experimental study *Proc. R. Soc.* A **388** 249–71
[16] Wierzchowski W and Moore M 2007 Bragg-case K_g and K_0 beam double-crystal synchrotron studies of growth sectors and dislocations in synthetic diamonds *J. Appl. Phys.* **101** 053518
[17] Lang A R 1959 The projection topograph: a new method in x-ray diffraction microradiography *Acta Crystallogr.* **12** 249–50
[18] Moore M and Lang A R 1972 On the internal structure of natural diamonds of cubic habit *Phil. Mag.* **26** 1313–25
[19] Moore M and Lang A R 1974 On the origin of the rounded dodecahedral habit of natural diamond *J. Cryst. Growth* **26** 133–9
[20] Machado W G, Moore M and Woods G S 1985 On the dodecahedral growth of coated diamonds *J. Cryst. Growth* **71** 718–27
[21] Fritsch E, Moore M, Rondeau B and Waggett R G 2005 X-ray topography of a natural twinned diamond of unusual pseudo-tetrahedral morphology *J. Cryst. Growth* **280** 279–85
[22] Rondeau B, Fritsch E, Moore M, Thomassot E and Sirakian J-F 2007 On the growth of natural octahedral diamond upon a fibrous core *J. Cryst. Growth* **304** 287–93
[23] Yacoot A and Moore M 1993 X-ray topography of natural tetrahedral diamonds *Miner. Mag.* **57** 223–30
[24] Yacoot A, Moore M and Makepeace A P W 1990 X-ray studies of synthetic radiation-counting diamonds *Phys. Med. Biol.* **35** 1409–22
[25] Frank F C and Lang A R 1965 X-ray topography of diamond *Physical Properties of Diamond* ed R Berman (Oxford: Oxford University Press) pp 69–115 and 425–6
[26] Wierzchowski W K, Moore M, Makepeace A P W and Yacoot A 1991 X-ray topographic studies and measurement of lattice parameter differences within synthetic diamonds grown by the reconstitution technique. *J. Cryst. Growth* **114** 209–27
[27] Haruta K 1965 New method of obtaining stereoscopic pairs of x-ray diffraction topographs *J. Appl. Phys.* **36** 1789–90
[28] Moore M and Wierzchowski W 1999 Transmission double-crystal synchrotron studies of synthetic diamond using the Haruta stereo-pairs technique *Phil. Trans. R. Soc.* A **357** 2671–9
[29] Lang A R, Moore M and Walmsley J C 1992 Diffraction and imaging studies of diamond *The Properties of Natural and Synthetic Diamond* ed J E Field (London: Academic) chapter 5, pp 213–58
[30] Lang A R, Makepeace A P W, Moore M and Machado W G 1983 On the variation of x-ray diffraction contrast with wavelength: a study with synchrotron radiation *J. Appl. Crystallogr.* **16** 113–25

[31] Machado W G, Moore M and Yacoot A 1998 Twinning in natural diamond. II. Interpenetrant cubes *J. Appl. Crystallogr.* **31** 777–82
[32] Yacoot A, Moore M and Machado W G 1998 Twinning in natural diamond. I. Contact twins *J. Appl. Crystallogr.* **31** 767–76
[33] Wierzchowski W and Moore M 1995 Bragg-case images of stacking faults *Acta Crystallogr.* A **51** 831–40
[34] Kowalski G, Lang A R, Makepeace A P W and Moore M 1989 Studies of stacking-fault contrast by synchrotron x-ray section topography *J. Appl. Crystallogr.* **22** 410–30
[35] Moore M and Lang A R 1972 An x-ray topographic study of impurity platelet distribution and size in an inhomogeneous diamond *Phil. Mag.* **25** 219–27
[36] Raman C V and Nilakantan P 1940 Reflexion of x-rays with change of frequency. Part II. The case of diamond *Proc. Indian Acad. Sci.* A **11** 389–97
[37] Lonsdale K and Milledge H J 1965 X-ray diffraction studies on diamond and some related materials *Physical Properties of Diamond* ed R Berman (Oxford: Oxford University Press) pp 12–68 and 423–5
[38] Clackson S G and Moore M 1989 Impurity platelets in diamond and x-ray spike topography *Indust. Diamond Rev.* **49** 128–33
[39] Moore M, Waggett R G, Wierzchowski W K and Makepeace A P W 1993 Synchrotron spike topography of natural type Ia diamond *Diamond Relat. Mater.* **2** 115–20
[40] Moore M and Lang A R 1977 The use of integrals of the Airy diffraction intensity profile in x-ray topography of 'spike' diffuse reflexions *J. Appl. Crystallogr.* **10** 422–5
[41] Evans T 1965 Transmission electron microscopy of diamond *Physical Properties of Diamond* ed R Berman (Oxford: Oxford University Press) pp 116–34 and 426–7
[42] Clackson S G, Moore M, Walmsley J C and Woods G S 1990 The relation between platelet size and the frequency of the B′ infrared absorption peak in type Ia diamond *Phil. Mag.* B **62** 115–28
[43] Bowen D K and Tanner B K 1998 *High-Resolution X-Ray Diffractometry and Topography* (London: Taylor and Francis (Abingdon))
[44] Lang A R, Kowalski G, Makepeace A P W and Moore M 1991 On long-range lattice perfection in natural type Ia diamond *Phil. Mag.* **64** 543–60
[45] Nailer S G, Moore M, Chapman J and Kowalski G 2007 On the role of nitrogen in stiffening the diamond structure *J. Appl. Crystallogr.* **40** 1146–52
[46] Kowalski G, Moore M, Gledhill G A and Maricic Z B 1996 Double-crystal diffractometric and topographic studies of (111) oriented synthetic diamonds *J. Phys. D: Appl. Phys.* **29** 793–800
[47] Lang A R, Moore M, Wierzchowski W K, Makepeace A P W and Welbourn C M 1991 On the dilatation of synthetic type Ib diamond by substitutional nitrogen impurity *Phil. Trans. R. Soc.* A **337** 497–520
[48] Kowalski G, Moore M, Gledhill G A and Maricic Z B 1996 Synchrotron x-ray studies of strain in (100) oriented HP/HT synthetic diamonds *Diamond Relat. Mater.* **5** 1254–63
[49] Murphy B M, Collins S P, Golshan M, Moore M, Reid J S and Kowalski G 2001 SRS station 16.3: high-resolution applications *Nucl. Instrum. Methods Phys. Res.* A **468** 1014–8
[50] Fewster P F 1996 Reciprocal-space mapping *X-Ray and Neutron Dynamical Diffraction Theory and Applications* ed A Authier, S Lagomarsino and B K Tanner (New York: Plenum) pp 269–88
[51] Moore M, Golshan M, Kowalski G, Reid J S, Collins S P and Murphy B M 1999 Reciprocal-space mapping of synthetic and natural diamond *J. Phys. D: Appl. Phys.* **32** A37–41
[52] Golshan M, Fewster P F, Andrew N L, Kidd P, Moore M and Butler J E 2001 Three-dimensional reciprocal-space mapping of chemical vapour deposited diamond *J. Phys. D: Appl. Phys.* **34** A44–6
[53] Petrashov V T, Moore M, Sosnin I A, Cox I S and Nilsson B 1999 Nanofabrication with highly collimated synchrotron radiation *Scientific Reports 1997–98* Synchrotron Radiation Department, CLRC Daresbury Laboratory 354-355
[54] Petrashov V T, Chua K G, Marshall K M, Shaikhaidarov R Sh and Nicholls J T 2005 Andreev probe of persistent current states in superconducting quantum circuits *Phys. Rev. Lett.* **95** 147001